Space Weather

RESEARCH ARTICLE
10.1029/2021SW002858

Real-Time Monitoring of Ionosphere VTEC Using Multi-GNSS Carrier-Phase Observations and B-Splines

Eren Erdogan[1], Michael Schmidt[1], Andreas Goss[1], Barbara Görres[2], and Florian Seitz[1]

[1]Deutsches Geodätisches Forschungsinstitut der Technischen Universität München (DGFI-TUM), München, Germany, [2]Bundeswehr Geoinformation Center (BGIC), Euskirchen, Germany

Key Points:

- A new real-time approach estimating simultaneously coefficients of the B-spline representation and biases of carrier-phases was introduced
- Carrier-phase observations from GPS, GLONASS, and GALILEO were incorporated into an adaptive Kalman filter
- Global Navigation Satellite Systems (GNSS) observations were obtained in Radio Technical Commission for Maritime Services format via the International GNSS Service real-time service

Correspondence to:
E. Erdogan,
eren.erdogan@tum.de

Citation:
Erdogan, E., Schmidt, M., Goss, A., Görres, B., & Seitz, F. (2021). Real-time monitoring of ionosphere VTEC using multi-GNSS carrier-phase observations and B-splines. *Space Weather*, *19*, e2021SW002858. https://doi.org/10.1029/2021SW002858

Received 22 JUL 2021
Accepted 21 SEP 2021

Abstract Monitoring the Vertical Total Electron Content (VTEC) of the ionosphere is important for applications ranging from navigation to detection of space weather events. Therefore, emerging efforts have been made by several analysis centers to estimate the VTEC using different approaches in real-time. Global Navigation Satellite Systems (GNSS) is a crucial technology for ionosphere modeling due to its worldwide distributed receivers, high temporal resolution, and low latency data dissemination capability. The selection of a convenient approach to extract ionosphere information from GNSS and the representation of VTEC by an appropriate mathematical model are essential factors for providing fast and accurate ionosphere products. Contrarily to the widespread phase-leveling method, which uses noisy and erroneous code measurements, the modeling concept in this paper utilizes pure carrier-phase measurements. Measurements acquired through the International GNSS Service (IGS) real-time service in Radio Technical Commission for Maritime Services format are from GPS, GLONASS, and GALILEO. The measurement biases, including the ambiguity of carrier-phase measurements, are simultaneously estimated along with VTEC model parameters. In our approach, VTEC is represented by B-spline expansions embedded into a Kalman filter. Due to their localizing feature, B-splines form a highly sparse structure in the filter measurement model. Thus, matrix operations for large-scale problems can be performed fast using sparse matrix operations, as is done in this study. The differential slant total electron content (dSTEC) analysis and the comparison with Jason-3 altimetry VTEC were performed for validation within selected periods in 2019. The dSTEC analysis shows that the quality of the generated real-time VTEC maps slightly outperforms those provided by the other IGS analysis centers.

Plain Language Summary As part of the Earth's upper atmosphere, the ionosphere is coupled to the Sun and the Earth's lower atmosphere by complex electromagnetic and dynamic interactions of charged particles (electrons and ions) and neutral species. Spatio-temporal variations of the ionosphere electron content are of particular importance for technologies utilizing electromagnetic signals such as navigation and telecommunication since the electromagnetic waves are refracted/reflected while traveling through the ionosphere. There has been an increasing demand for real-time ionosphere products to compute interactions between electromagnetic waves and the ionosphere in real-time. In this context, the IGS and its several analysis centers have been developing models to provide global Vertical Electron Content (VTEC) products using different approaches based on Global Navigation Satellite Systems (GNSS) observations. By considering the crucial impact of the ionosphere and its constituents on our life, in this study, we model the ionosphere VTEC represented by B-splines embedded into a Kalman filter in real-time using carrier-phase observations from geodetic GNSS receivers.

1. Introduction

Real-time monitoring of the ionospheric plasma distribution and associated irregularities is of increasing importance for users of the Global Navigation Satellite Systems (GNSS) in various fields such as telecommunication, positioning, navigation, aviation, natural disaster monitoring and warning. It is also vital to monitor the ionosphere in real-time for forecasting space weather events. Rapid technological advances in the fast transmission of big data allow for generating and disseminating the essential ionosphere parameters, including the spatio-temporal variations of the Vertical Total Electron Content (VTEC), with low latency. The International GNSS Service (IGS) and its Ionosphere Associated Analysis Centers have been continuously providing Global Ionosphere Maps (GIMs) with improving resolution, accuracy, and latency since 1998 (Hernández-Pajares et al., 2009). By following the launch of the experimental IGS International

Real-Time Service (Caissy et al., 2012), several analysis centers have focused on modeling VTEC in real-time and combining VTEC products derived from different real-time approaches; see Li et al. (2020) for an overview. The IGS service allows for accessing real-time data in Radio Technical Commission for Maritime Services (RTCM) format from a global network of GNSS receivers with a latency of up to a few seconds. By this motivation, we focus in the following on introducing a new approach for real-time VTEC modeling based on the B-spline representation of global VTEC by ingesting solely carrier-phase observations from the GPS, GLONASS, and GALILEO constellations into an adaptive Kalman filter. The simultaneous estimation of all unknown ionosphere parameters comprising B-spline coefficients and biases of the carrier-phase measurements was carried out in real-time for the first time in this study.

The accuracy of VTEC models varies according to the handling of carrier-phase ambiguities, satellite/receiver biases, spherical shell specifications, and mathematical approaches for the VTEC representation (Banville et al., 2011). The ionospheric information, that is, the slant total electron content (STEC), can be extracted from the geometry-free combination of GNSS signals at distinct frequencies. The pseudo-range (code) ionosphere combination generates unambiguous but rather noisy information. On the other hand, the carrier-phase ionosphere combination is about two orders of magnitude more precise, but it is biased by an unknown number of phase cycles (see, Hofmann-Wellenhof et al., 2008; Rovira-Garcia et al., 2016). The leveling technique is a widely used method to remove the ambiguity biases in carrier-phase observations with the aid of code observations (Mannucci et al., 1993, 1998). Although this method is capable of eliminating the biases, the leveled observations are contaminated by significant errors up to several TEC units due to the high noise level, time-varying inter-frequency biases, and multi-path effects introduced by code observations (Ciraolo et al., 2007). Alternative approaches based solely on carrier-phase observations or precise point positioning (PPP) techniques have been used to avoid the leveling procedure, see Hernández-Pajares et al. (2011). The studies of Banville et al. (2011, 2012), Chen et al. (2018) and Xiang et al. (2019) demonstrated that the accuracy of STEC observations could significantly be improved by removing the phase ambiguities derived from a PPP solution compared to those obtained from the standard leveling approach. Plenty of methods relying on PPP techniques have been introduced to extract accurate ionospheric information from (un)differenced and (un)combined GNSS observations (see, e.g., T. Liu et al., 2018; Ren et al., 2020; Xiang et al., 2017; Zhang, 2016). The main drawback of many PPP-based ionosphere solutions is the requirement for precise auxiliary information, which usually includes, for example, satellite orbits, clock data, and even reference station coordinates in some studies. This requirement introduces another challenging task of obtaining the auxiliary data precisely and reliably in real-time.

As mentioned above, to avoid the leveling procedure, the phase biases can also be obtained along with other ionospheric target parameters by solely utilizing the ionosphere combination of carrier-phase observations. For instance, this approach was carried to estimate the global electron density distribution by employing a voxel-based tomographic model; see, Hernández-Pajares et al. (1999). Brunini and Azpilicueta (2009) analyzed the effect of the leveling technique and modeling errors on the calibration of STEC biases. The VTEC model used in their evaluations is based on the thin shell assumption and bi-quadratic expansions defined over a given receiver. They showed that the bias calibration using the phase leveling approach dominantly suffers from both the leveling and model errors. However, the use of the carrier-phase ionosphere combination alone is free of leveling error, and therefore, the modeling error is the primary source contributing to the total error budget. Another study for the STEC bias calibration based on carrier-phase observations was presented by Krypiak-Gregorczyk and Wielgosz (2018). This approach was employed to estimate the carrier-phase biases in a pre-processing step by the method of least squares, and in the following step, the calibrated STEC observations were utilized to generate the VTEC distribution over Europe using a thin-plate-splines approximation (Krypiak-Gregorczyk et al., 2017).

In this study, we also solely utilize carrier-phase observations for real-time VTEC modeling. Instead of calibrating the observations in a pre-processing step, the presented approach simultaneously estimates the carrier-phase biases and the B-spline model coefficients by the Kalman filter running in real-time. Raw carrier-phase observations are from GPS, GLONASS, and GALILEO and were acquired in RTCM format from the IGS real-time service.

In addition to incorporating precise observations, the selection of the mathematical model describing the spatial distribution of electron content is of great importance. Various models have been introduced for

global VTEC representation, for instance, B-Spline series expansion (Schmidt, 2007; Schmidt et al., 2015), spherical harmonic expansion (Schaer, 1999), TEC values on triangular tiles (Mannucci et al., 1998) and grids (Skone, 1999), BMARS (Durmaz & Karslioglu, 2015), thin-plate spline representation (Krypiak-Gregorczyk et al., 2017) as well as multi-dimensional models, see, for example, Farzaneh and Forootan (2017), Gerzen et al. (2020), Hernández-Pajares et al. (1999), Z. Liu (2004), Limberger (2015), Schmidt et al. (2015), and Zeilhofer et al. (2009). We refer to, for example, Erdogan et al. (2020), Jerez et al. (2020), Roma-Dollase et al. (2018) for the comparison of various final and (ultra) rapid VTEC products derived from different approaches, and Li et al. (2020), Ren et al. (2019) for real-time products.

For VTEC and electron density modeling, B-splines yield a very powerful mathematical tool to deal with the heterogeneous data distribution and data gaps because of its localizing property (Schmidt et al., 2015). For example, Schmidt et al. (2011) showed that a large data gap at a region results in a dramatic global quality degradation in the estimated VTEC map due to artificial oscillating structures when a spherical harmonic (SH) expansion, which is of global support, is employed. Contrarily, in the same study, the artificial structures appear only in the close neighborhood of the data gap when the localizing B-spline expansion replaces the SH representation. The B-splines also support the construction of a multi-scale representation of signals, which paves the way for effective data compression techniques (Lyche & Schumaker, 2000; Schmidt, 2012). Moreover, the coefficients of the B-spline representation resemble global VTEC maps in terms of the spatio-temporal distribution and magnitude, which allow for inferring physical interpretations from the coefficients directly (Erdogan et al., 2020). B-splines were applied to model ionospheric variables in various studies, for instance, modeling regional VTEC (Durmaz & Karslioglu, 2015; Goss, Schmidt, et al., 2020; Nohutcu et al., 2010; Schmidt et al., 2008; Zeilhofer et al., 2009) and global VTEC (Dettmering et al., 2014; Erdogan et al., 2017, 2020; Goss et al., 2019; Schmidt et al., 2011), the computation of corrections to a climatological reference model such as IRI (Liang et al., 2015), the estimation of key parameters of the Chapman function for electron density modeling (Limberger et al., 2013), and the combination of different space geodetic techniques for VTEC modeling (Dettmering et al., 2011).

By taking advantage of the B-spline representation, Erdogan et al. (2017) presented an approach to sequentially estimate ultra-rapid global VTEC maps by a Kalman filter, which assimilates ionospheric observations extracted from the GPS and GLONASS via the conventional carrier-phase leveling technique. Later on, the sequential filtering approach was extended with adaptive methods to estimate the covariance matrices of the measurement and dynamics models in run-time (Erdogan et al., 2020) and then applied for regional VTEC modeling (Goss, Schmidt, et al., 2020). In this study, we incorporate the adaptive approach presented by Erdogan et al. (2020) into the real-time modeling of the spatio-temporal VTEC distribution using B-spline functions. GNSS data is acquired from the IGS real-time service and sequentially processed over time by the filter to simultaneously estimate coefficients of the B-spline representation and the carrier-phase biases.

As stated above, the presented approach estimates the carrier-phase biases for each phase connected arc defined between a GNSS receiver and satellite. As a result, a large number of bias parameters needs to be estimated, which can degrade the stability of the Kalman filter implementation. In order to cope with this problem, the measurement model was extended to incorporate supplementary information derived from a nowcast model. The nowcast model aims to increase the filter stability, supports the model over regions with large data gaps, and provides VTEC maps in case of losing the connection to data providers. The nowcast model is based on the combination of a trigonometric series and an ARMA model. It uses the time series of high-resolution ultra-rapid products of DGFI-TUM (see, e.g., Goss et al., 2019) as input data generated according to Erdogan et al. (2020).

This paper is outlined as follows. Section 2 explains the extraction of ionosphere information from real-time carrier-phase observations. In Section 3 the measurement model of the filter is presented. This section comprises the sub-parts: definition of the GNSS observation equations, B-spline representation of global VTEC, nowcasting of B-spline coefficients as supplementary information, and the overall measurement model. Section 4 shows the real-time estimation approach based on the adaptive Kalman filter implementation, the data editing procedures, and the overall procedures from an application point of view. Section 5 explains the validation techniques, and discusses the results. Finally, Section 6 provides the conclusion and future work.

2. GNSS Real-Time Ionosphere Measurements

For real-time applications, the GNSS data has been usually transmitted from GNSS receivers to users by casters through the Networked Transport of RTCM via Internet Protocol (NTRIP). NTRIP is a data transfer protocol that enables the streaming of GNSS data to stationary or mobile users via Internet (Weber et al., 2005). A list of GNSS NTRIP casters can be accessed, for example, from http://rtcm-ntrip.org/home.html. In this study, the data collected by IGS stations is downloaded through the IGS NTRIP caster (https://www.igs-ip.net/home) which is currently operated in support of the Real-Time IGS Working Group. The open-source software BNC provided by the Federal Agency for Cartography and Geodesy (BKG) as an NTRIP Client is executed to download data from the GNSS constellations (Weber et al., 2016). The downloaded data set includes carrier-phase observations from the L1 and L2 signals of GPS and GLONASS as well as the E1 and E5a signals of GALILEO. The challenging task in real-time modeling is to deal with high-rate raw GNSS data. Most receivers in the IGS caster provide data at a 1 Hz sampling rate. Since accomplishing the data processing and estimation steps in real-time in less than a second might not be possible in practice, a proper down-sampling is typically applied by considering the computational resources. In this study, the down-sampling rate is set to obtain raw data every 10 s.

Following the data download, the real-time data pre-processing step is carried out. First, the ionosphere combination

$$L^s_{r,k} = \Phi^s_{r,f_1,k} - \Phi^s_{r,f_2,k} \tag{1}$$

of carrier-phase observations is computed. Herein $L^s_{r,k}$ is the geometry-free ionosphere combination of the carrier-phases observations Φ^s_{r,f_1} and Φ^s_{r,f_2} in the meter unit, obtained from GNSS signals with the signal frequencies f_1 and f_2 (see, e.g., Hofmann-Wellenhof et al., 2008).

The ionosphere combinations (Equation 1) for each receiver-satellite pair are collected in an arc container. A cycle-slip detection algorithm based on two frequency carrier-phase data is separately applied to each arc to detect jumps in the signals; see, for example, Subirana et al. (2013). The algorithm utilizes the first-order time difference of the carrier-phase ionosphere combination. The difference of the consecutive observations on the same arc amplifies the jumps and therefore increases the possibility to detect the jumps (Hofmann-Wellenhof et al., 2008). Hence, the difference equation reads

$$\Delta L^s_{r,k} = (L^s_{r,k} - L^s_{r,k-1})/\Delta t_k \tag{2}$$

where $\Delta t_k = t_k - t_{k-1}$. The division by the time difference Δt_k aims at avoiding false jump detection due to a missing observation. From the time series $\Delta L^s_{r,k-n},\ldots,\Delta L^s_{r,k}$ along an arc, the predicted value of $\Delta L^{s,-}_{r,k+1}$ for the time moment t_{k+1} is calculated. The prediction is performed using a second-order polynomial function, and the coefficients of the polynomials are computed via a curve-fitting approach using the last, for example, 15 consecutive data points. If the difference between the real observation $\Delta L^s_{r,k+1}$ and the predicted value of $\Delta L^{s,-}_{r,k+1}$ exceeds the threshold ϵ, the data point on the arc at t_{k+1} is marked as a jump. Moreover, a data gap threshold of 120 s is also applied to mark time differences exceeding the threshold. It should be noted that a detected cycle-slip is not repaired; instead, a new arc is initiated. After the jump detection and the marking procedures, the ionosphere combinations $L^s_{r,k}$ are converted to TECU unit and then stored in a database.

3. Ionosphere Measurement Model

As mentioned before, the Kalman filter is carried out as a sequential estimator for real-time VTEC modeling. The following subsections explain the implementation details of the measurement model of the filter designed for real-time VTEC modeling.

3.1. Observation Equations

The geometry-free ionosphere combination (Equation 1) eliminates the non-dispersive effects, including the geometric line of sight distance between the satellite s and the receiver r as well as the receiver and satellite clock offsets, and can be written as

$$L^s_{r,k} = STEC_k + B_{r,k} + B^s_k + B_{\mathrm{A}^s_r,k} + e_k \tag{3}$$

where $STEC_k$ is the slant total electron content, $B_{r,k}$ and B^s_k refer to the frequency-dependent receiver and satellite inter-frequency biases (IFB), the combined ambiguity bias of a carrier-phase observation is denoted by $B_{A^s_r,k}$, and e_k stands for the measurement error; see, for example, Ciraolo et al. (2007), Brunini and Azpilicueta (2009), Erdogan et al. (2017). The error term e_k comprises the measurement noise and the other effects such as multi-path and thermal disturbance.

For the sake of clarity, the ionosphere combination Equation 3 is re-written for each of the GNSS satellites as the observation equation

$$\begin{aligned} y_{\mathrm{GPS},k} &= m(z^s_{r,k}) \cdot VTEC_k + C^s_{r,\mathrm{GPS},k} + e_{\mathrm{GPS},k} \\ y_{\mathrm{GLO},k} &= m(z^s_{r,k}) \cdot VTEC_k + C^s_{r,\mathrm{GLO},k} + e_{\mathrm{GLO},k} \\ y_{\mathrm{GAL},k} &= m(z^s_{r,k}) \cdot VTEC_k + C^s_{r,\mathrm{GAL},k} + e_{\mathrm{GAL},k}, \end{aligned} \tag{4}$$

where y_{GPS}, y_{GLO} and y_{GAL} are the ionospheric observations in TECU for GPS, GLONASS and GALILEO at time stamp k. The ionospheric term $STEC$ in Equation 3 is replaced by the Single Layer Model representation (see e.g., Schaer, 1999) and reads

$$STEC_k = m(z^s_{r,k}) \cdot VTEC_k, \tag{5}$$

where the mapping function m is depending on the satellite zenith angle $z^s_{r,k}$. The terms $C^s_{r,\mathrm{GPS},k}$, $C^s_{r,\mathrm{GLO},k}$ and $C^s_{r,\mathrm{GAL},k}$ refer to the total phase biases and consist of the IFBs and the carrier-phase ambiguity biases as given in Equation 3 and are defined as

$$C^s_{r,\mathrm{GNSS},k} = B_{r,k} + B^s_k + B_{A^s_r,k} \tag{6}$$

3.2. B-Spline Representation of Global VTEC

The global VTEC distribution in Equation 4 is represented by the tensor product expansion

$$VTEC_k = VTEC(\varphi,\lambda,t_k) = \sum_{k_1=0}^{K_{J_1}-1} \sum_{k_2=0}^{K_{J_2}-1} d^{J_1,J_2}_{k_1,k_2}(t_k)\, N^2_{J_1,k_1}(\varphi)\, T^3_{J_2,k_2}(\lambda), \tag{7}$$

where $d^{J_1,J_2}_{k_1,k_2}(t_k)$ stands for the time-dependent B-spline coefficients (Schmidt et al., 2015). The basis functions along the latitude φ are defined by the polynomial B-spline functions $N^2_{J_1,k_1}(\varphi)$ of degree 2 whereas $T^3_{J_2,k_2}(\lambda)$ are the trigonometric B-splines of order 3 defined as a function of longitude λ (Lyche & Schumaker, 2000; Schumaker & Traas, 1991). The parameters k_1 and k_2 refer to the geometrical positions of the knot locations on the sphere. The spatial resolution of the model is controlled by the levels of J_1 and J_2. The number of polynomial B-spline functions in the latitude direction for the level J_1 is given by $K_{J_1} = 2^{J_1} + 2$, and $K_{J_2} = 3 \cdot 2^{J_2}$ refers to the number of trigonometric B-splines in the longitude direction for the level J_2. Accordingly, the total number of the series coefficients associated with the tensor-product B-splines is computed by $K_{J_1} \cdot K_{J_2}$.

The global VTEC representation (Equation 7) requires a properly handling of constraints to preserve spherical geometry. Two sets of constraint equations, namely the pole equality and the pole continuity, are introduced for the B-spline model representing a function defined on the sphere (Lyche & Schumaker, 2000). Accordingly, the overall constraint equation reads

$$\mathbf{X}_{d_{\mathrm{MC}},k}\,\mathbf{d}_k = \mathbf{y}_{\mathrm{MC},k} \tag{8}$$

where $\mathbf{X}_{d_{\mathrm{MC}},k}$ is a known matrix, $\mathbf{y}_{\mathrm{MC},k}$ equals to zero vector and the vector $\mathbf{d}_k$ comprises the B-spline coefficients.

Taking the dominant drivers into account for selecting an appropriate coordinate system is important to model ionosphere phenomena (Laundal & Richmond, 2016). The Earth's magnetic field has an essential role in forming the ionospheric electron distribution and the equatorial ionization anomaly. The Sun is the main driver for the spatio-temporal variation of the photo-ionization process. Therefore, a solar magnetic coordinate system is adapted for the representation of the global VTEC model (Equation 7); for further implementation details, we refer to Erdogan et al. (2020).

3.3. Nowcasted B-Spline Coefficients as Supplementary Information

Data gaps due to the heterogeneous GNSS data distribution and the large size of unknown parameters typically make estimators vulnerable to numerical problems, such as ill-conditioning and filter instability. The global real-time approach is extended by supplementary information to keep the Kalman filter numerically stable and to enhance the estimation quality at regions suffering from large data gaps. Furthermore, the supplementary information can be considered as a background ionosphere model providing homogeneous observations to support the real-time model over the oceans where the filter usually suffers from a lack of enough observations. Moreover, it feeds the estimator in case of interruptions in the real-time data streams, for example, due to loss of the connection to data providers.

The supplementary information is obtained in the form of B-spline coefficients from the ultra-rapid global VTEC product of DGFI-TUM with a latency of less than 3 hr (see, e.g., Erdogan et al., 2020; Goss et al., 2019). Because of its dissemination latency, the supplementary information is incorporated into real-time modeling via a nowcast model.

The nowcast model comprises a stochastic and a deterministic part. A linear trend (LT) model and a trigonometric series (TS) are chosen to represent the deterministic part in the time series of B-spline coefficients. An ARMA process consisting of an auto-regressive polynomial of order p and a moving average polynomial of order q is executed for the stochastic part. The overall nowcast model reads

$$\begin{aligned} d^{J_1,J_2}_{k_1,k_2,\mathrm{NC}}(t_k) = &\left\{c_0 + c_1 \cdot t_k\right\}^{\mathrm{LT}}_{k_1,k_2} \\ &+\left\{\sum_{i=1}^{N}(a_i \cdot \cos(\omega_i t_k) + b_i \cdot \sin(\omega_i t_k))\right\}^{\mathrm{TS}}_{k_1,k_2} \\ &+\left\{Z_{t_k} + \sum_{m=1}^{q}(\phi_k \cdot Z_{t_{k-m}}) + \sum_{l=0}^{p}(\theta_k \cdot X_{t_{k-l}})\right\}^{\mathrm{AR}}_{k_1,k_2} \end{aligned} \tag{9}$$

where the first term refers to LT model consisting of the coefficients c_0 and c_1. The term $\{\cdot\}^{TS}_{k_1,k_2}$ refers to the trigonometric model including the series coefficients $a_1,\ldots,a_N$ and $b_1,\ldots,b_N$ with the known periods $T_i = 2\pi/\omega_i$. The term $\{\cdot\}^{AR}_{k_1,k_2}$ stands for the ARMA process including the coefficients $\phi_1,..,\phi_p$ and $\theta_1,\ldots,\theta_q$ of the auto-regressive part and the moving-average part, respectively. Moreover, the parameters X_{t_k} and Z_{t_k} are the residual signal and the error terms, respectively.

The coefficients of the nowcast model are determined for each B-spline coefficient independently. First, the LT and TS coefficients are computed by fitting the deterministic model $\{\cdot\}^{LT}_{k_1,k_2} + \{\cdot\}^{TS}_{k_1,k_2}$ to the input time series of a B-spline coefficient. Next, the residual signal, which is obtained by subtracting the deterministic signal from the input signal, is used to compute the coefficients of the ARMA model $\{\cdot\}^{AR}_{k_1,k_2}$. The overall estimation procedure is repeated every hour to keep the parameters of the nowcast model up to date. Once the coefficients are estimated, the nowcasted B-spline coefficients $\mathbf{d}_{\mathrm{NC},k}$ are obtained by extrapolating Equation 9 to the present time. The nowcasted coefficients are considered in real-time modeling as a vector of supplementary observations $\mathbf{y}_{\mathrm{NC},k}$ given as

$$\mathbf{y}_{\mathrm{NC},k} = \mathbf{d}_{\mathrm{NC},k} \tag{10}$$

3.4. Measurement Model

The measurement model of the Kalman filter is constructed from the observation Equation 4 for each GNSS satellite, the constraint Equation 8, and the supplementary information derived from the nowcast model (Equation 10). The measurement model reads

$$\mathbf{y}_k = \mathbf{X}_k \boldsymbol{\beta}_k + \mathbf{e}_k \tag{11}$$

where $\mathbf{y}_k$ is the measurement vector, $\mathbf{X}_k$ is the design matrix, $\boldsymbol{\beta}_k$ denotes the vector of B-spline coefficients, and $\mathbf{e}_k$ is the error vector. The measurement vector $\mathbf{y}_k$ comprises the sub-vectors $\mathbf{y}_{\mathrm{GPS},k}$, $\mathbf{y}_{\mathrm{GLO},k}$, $\mathbf{y}_{\mathrm{GAL},k}$, $\mathbf{y}_{\mathrm{NC},k}$ and $\mathbf{y}_{\mathrm{MC},k}$. The constraint Equation 8 is handled by the method of perfect measurements and therefore the sub-vector $\mathbf{y}_{\mathrm{MC},k}$ is considered as measured (see, e.g., Simon, 2010). The state vector $\boldsymbol{\beta}_k$ consists of the

sub-vector $\mathbf{d}_k = (d_{k_1,k_2}^{J_1,J_2}(t_k))$ of the unknown B-spline coefficients $d_{k_1,k_2}^{J_1,J_2}(t_k)$ and the sub-vectors $\mathbf{c}_{r,\mathrm{GPS},k}^s$, $\mathbf{c}_{r,\mathrm{GLO},k}^s$ and $\mathbf{c}_{r,\mathrm{GAL},k}^s$ of the arc biases (Equation 6). Consequently, the state vector $\boldsymbol{\beta}_k$ and the observation vector $\mathbf{y}_k$ is defined by

$$\boldsymbol{\beta}_k^{\mathrm{T}} = \begin{bmatrix} \mathbf{d}_k^{\mathrm{T}} & (\mathbf{c}_{r,\mathrm{GPS},k}^s)^{\mathrm{T}} & (\mathbf{c}_{r,\mathrm{GLO},k}^s)^{\mathrm{T}} & (\mathbf{c}_{r,\mathrm{GAL},k}^s)^{\mathrm{T}} \end{bmatrix} \tag{12}$$

$$\mathbf{y}_k^{\mathrm{T}} = \begin{bmatrix} \mathbf{y}_{\mathrm{GPS},k}^{\mathrm{T}} & \mathbf{y}_{\mathrm{GLO},k}^{\mathrm{T}} & \mathbf{y}_{\mathrm{GAL},k}^{\mathrm{T}} & \mathbf{y}_{\mathrm{NC},k}^{\mathrm{T}} & \mathbf{y}_{\mathrm{MC},k}^{\mathrm{T}} \end{bmatrix} \tag{13}$$

The corresponding design matrix $\mathbf{X}_k$ in Equation 11 is given as

$$\mathbf{X}_k = \begin{bmatrix} \mathbf{X}_{y_{\mathrm{GPS}},k} \\ \mathbf{X}_{y_{\mathrm{GLO}},k} \\ \mathbf{X}_{y_{\mathrm{GAL}},k} \\ \mathbf{X}_{y_{\mathrm{NC}},k} \\ \mathbf{X}_{y_{\mathrm{MC}},k} \end{bmatrix} = \begin{bmatrix} \mathbf{X}_{d_{\mathrm{GPS}},k} & \mathbf{X}_{C_{\mathrm{GPS}},k} & \mathbf{0} & \mathbf{0} \\ \mathbf{X}_{d_{\mathrm{GLO}},k} & \mathbf{0} & \mathbf{X}_{C_{\mathrm{GLO}},k} & \mathbf{0} \\ \mathbf{X}_{d_{\mathrm{GAL}},k} & \mathbf{0} & \mathbf{0} & \mathbf{X}_{C_{\mathrm{GAL}},k} \\ \mathbf{X}_{d_{\mathrm{NC}},k} & \mathbf{0} & \mathbf{0} & \mathbf{0} \\ \mathbf{X}_{d_{\mathrm{MC}},k} & \mathbf{0} & \mathbf{0} & \mathbf{0} \end{bmatrix} \tag{14}$$

herein, $\mathbf{X}_{d_{\mathrm{GPS}},k}$, $\mathbf{X}_{d_{\mathrm{GLO}},k}$ and $\mathbf{X}_{d_{\mathrm{GAL}},k}$ are the design sub-matrices for GPS, GLONASS and GALILEO with respect to the vector $\mathbf{d}_k$ of the unknown B-spline coefficients. The design sub-matrices for the arc biases of GPS, GLONASS and GALIELO are $\mathbf{X}_{C_{\mathrm{GPS}},k}$, $\mathbf{X}_{C_{\mathrm{GLO}},k}$ and $\mathbf{X}_{C_{\mathrm{GAL}},k}$. The matrix $\mathbf{X}_{d_{\mathrm{NC}},k}$ refers to the design matrix of the nowcasted observation and is equivalent to the identity matrix. $\mathbf{X}_{d_{\mathrm{MC}},k}$ stands for the design matrix of the constraint Equation 8.

The diagonal covariance matrix of the measurement model $\boldsymbol{\Sigma}_{y,k}$ consists of the components $\boldsymbol{\Sigma}_{y_{\mathrm{GPS}},k}$, $\boldsymbol{\Sigma}_{y_{\mathrm{GLO}},k}$, $\boldsymbol{\Sigma}_{y_{\mathrm{GAL}},k}$, $\boldsymbol{\Sigma}_{y_{\mathrm{NC}},k}$ and $\boldsymbol{\Sigma}_{y_{\mathrm{MC}},k}$ describing the measurement model uncertainties for the GPS, GLONASS and GALILEO observations as well as the nowcasted and perfect measurements, respectively. The covariance matrix $\boldsymbol{\Sigma}_{y_{\mathrm{NC}},k}$ is derived from the nowcast model. The covariance matrix of the perfect measurements $\boldsymbol{\Sigma}_{y_{\mathrm{MC}},k}$ is a diagonal matrix, and, in practice, its diagonal components are usually set to very small values to avoid numerical problems (see, e.g., Erdogan et al., 2020; Koch, 1999; Teixeira et al., 2009). Consequently, the covariance matrix $\boldsymbol{\Sigma}_{y,k}$ is given by

$$\boldsymbol{\Sigma}_{y,k} = \mathrm{diag}\left(\boldsymbol{\Sigma}_{y_{\mathrm{GPS}},k},\ \boldsymbol{\Sigma}_{y_{\mathrm{GLO}},k},\ \boldsymbol{\Sigma}_{y_{\mathrm{GAL}},k},\ \boldsymbol{\Sigma}_{y_{\mathrm{NC}},k},\ \boldsymbol{\Sigma}_{y_{\mathrm{MC}},k}\right) \tag{15}$$

where "diag" is the block-diagonal matrix operator, for example, $diag(\mathbf{A},\mathbf{B}) = \begin{bmatrix} \mathbf{A} & \mathbf{0} \\ \mathbf{0} & \mathbf{B} \end{bmatrix}$.

4. Estimation of Ionospheric Target Parameters

4.1. Sequential Filtering

The estimation of the ionospheric target parameters is carried out using the Kalman filter (Kalman, 1960) which provides an optimal estimator in terms of, for example, minimum variance estimation when the system of equations is linear and the model uncertainties have a Gaussian distribution; see, for example, Jazwinski (2007). The Kalman filter has been widely preferred for (near) real-time applications due to its recursive nature. It does not require the storage of past data and allows for an immediately updating of the unknown parameters upon the reception of new measurements. The Kalman filter extended by self-learning adaptive approaches can be carried out to estimate the covariance matrices or their parameters during the filter run-time, see Brown and Hwang (2012), Hide et al. (2004), Mehra (1972).

In this study, we employ the adaptive Kalman filter implementation developed by Erdogan et al. (2020) for VTEC modeling. Accordingly, the Kalman Filter consists of a prediction step (time update) and a correction step (measurement update), and these two steps are repeatedly executed over time. The prediction equations between the consecutive epochs t_k and t_{k-1} read

$$\boldsymbol{\Sigma}_{\beta,k}^{-} = \mathbf{F}_k \hat{\boldsymbol{\Sigma}}_{\beta,k-1} \mathbf{F}_k^T + \boldsymbol{\Sigma}_{w,k}, \tag{16}$$

$$\boldsymbol{\beta}_k^{-} = \mathbf{F}_k \hat{\boldsymbol{\beta}}_{k-1} \tag{17}$$

where $\boldsymbol{\beta}_k^{-}$ and $\boldsymbol{\Sigma}_{\beta,k}^{-}$ are the predicted state vector and the associated predicted covariance matrix, the term $\mathbf{F}_k$ refers to the state transition matrix, and $\boldsymbol{\Sigma}_{w,k}$ stands for the process noise covariance matrix (see, e.g.,

Gelb, 1974; Grewal & Andrews, 2008). Since the VTEC distribution is presented in the solar magnetic coordinate system, the effect of the Earth's diurnal motion in the temporal variation of the B-spline coefficients is mitigated due to the Sun alignment (see, e.g., Erdogan et al., 2017). The solar alignment allows the ionosphere to be treated as stationary (Hansen, 1998). Moreover, the carrier-phase biases, including the ambiguity biases and IFBs are stable over time. Therefore, the ionospheric variables in the time domain can be represented by a simple stochastic model, that is, the random walk process; see, for example, Mannucci et al. (1998). Accordingly, the state transition matrix $\mathbf{F}_k$ is set to an identity matrix, that is, $\mathbf{F}_k = \mathbf{I}$. The process noise covariance matrix $\mathbf{\Sigma}_{w,k}$ is defined as

$$\mathbf{\Sigma}_{w,k} = \mathrm{diag}\left(\mathbf{\Sigma}_{w_d,k}, \quad \mathbf{\Sigma}_{w_{C_r^s},k} \right) \tag{18}$$

where $\mathbf{\Sigma}_{w_d,k}$ and $\mathbf{\Sigma}_{w_{C_r^s},k}$ are diagonal matrices, and they refer to the process noise covariance matrices of the B-spline coefficients and carrier-phase biases, respectively. Each diagonal component of $\mathbf{\Sigma}_{w_d,k}$ varies in time with respect to the magnitude and spatial distribution of VTEC, which is computed in a self-adaptive manner during run-time of the filter as described by Erdogan et al. (2020). The matrix $\mathbf{\Sigma}_{w_{C_r^s},k}$ is simply defined as $\mathbf{\Sigma}_{w_{C_r^s},k} = \sigma^2_{C_r^s}\mathbf{I}$. The variance factor $\sigma^2_{C_r^s}$ is set to an experimentally defined value to compensate the dynamic model errors and to keep the filter sensitive to observations.

The subsequent measurement update step of the Kalman Filter is executed following the time update step by considering the new information described by the measurement model (Equation 11) to correct the predicted state vector and covariance matrix obtained from the Equations 16 and 17. In this study, an alternative version of the update equations is employed as

$$\hat{\mathbf{\Sigma}}_{\beta,k} = \left(\sum_{j=1}^{q} \frac{1}{\sigma^2_{y_j,k}} \mathbf{X}^T_{y_j,k} \mathbf{P}_{y_j,k} \mathbf{X}_{y_j,k} + (\mathbf{\Sigma}^-_{\beta,k})^{-1} \right)^{-1}, \tag{19}$$

$$\hat{\boldsymbol{\beta}}_k = \hat{\Sigma}_{\beta,k} \cdot \left(\sum_{j=1}^{q} \frac{1}{\sigma^2_{y_j,k}} \mathbf{X}^T_{y_j,k} \mathbf{P}_{y_j,k} \mathbf{y}_{y_j,k} + (\mathbf{\Sigma}^-_{\beta,k})^{-1} \boldsymbol{\beta}^-_k \right) \tag{20}$$

where $\hat{\boldsymbol{\beta}}_k$ and $\hat{\mathbf{\Sigma}}_{\beta,k}$ are the updated parameters computed by incorporating the new observations $\mathbf{y}_{y_j,k}$ marked by the index $j \in \{1,\ldots,q\}$ (Erdogan et al., 2020). In this study, we choose $q = 5$ for $\mathbf{y}_{\mathrm{GPS},k}$, $\mathbf{y}_{\mathrm{GLO},k}$, $\mathbf{y}_{\mathrm{GAL},k}$, $\mathbf{y}_{\mathrm{NC},k}$ and $\mathbf{y}_{\mathrm{MC},k}$ in Equation 13. Similarly, the design sub-matrix $\mathbf{X}_{y_j,k}$ refers to $\mathbf{X}_{y_{\mathrm{GPS}},k}$, $\mathbf{X}_{y_{\mathrm{GLO}},k}$, $\mathbf{X}_{y_{\mathrm{GAL}},k}$, $\mathbf{X}_{y_{\mathrm{NC}},k}$ and $\mathbf{X}_{y_{\mathrm{MC}},k}$ in Equation 14. The variance component $\sigma^2_{y_j,k}$ stands for $\sigma^2_{y_{\mathrm{GPS}},k}$, $\sigma^2_{y_{\mathrm{GLO}},k}$, $\sigma^2_{y_{\mathrm{GAL}},k}$, $\sigma^2_{y_{\mathrm{NC}},k}$ and $\sigma^2_{y_{\mathrm{MC}},k}$ and is obtained by defining the sub-matrices of the covariance matrix (Equation 15) according to $\mathbf{\Sigma}_{y_j,k} = \sigma^2_{y_j,k} \cdot \mathbf{P}^{-1}_{y_j,k}$ with known positive definite weight matrices $\mathbf{P}_{y_j,k}$

The design matrices $\mathbf{X}_{y_j,k}$ in the Equations 19 and 20, which are sub-elements of $\mathbf{X}_k$ (Equation 14), are matrices of highly sparse structure. In particular, the sparsity of the matrices $\mathbf{X}_{d_{\mathrm{GPS}},k}$, $\mathbf{X}_{d_{\mathrm{GLO}},k}$ and $\mathbf{X}_{d_{\mathrm{GAL}},k}$ arises from the compact support of the B-spline functions. By considering this high sparsity as well as the large size of the design matrix (Equation 14), because of the unknown carrier-phase biases introduced for each satellite-receiver pair, the matrix and vector calculus with the sub-matrices $\mathbf{X}_{y_j,k}$ in Equations 19 and 20 has been carried out using sparse matrix techniques.

4.2. Data Editing

The predicted covariance matrix $\mathbf{\Sigma}^-_{\beta,k}$ and the predicted state vector $\boldsymbol{\beta}^-_k$ of the Kalman filter are required to be edited before performing the measurement update step. The components of the carrier-phase biases that are not valid at the epoch t_k due to loss of tracking, cycle-slips, or large data gaps are removed from $\mathbf{\Sigma}^-_{\beta,k}$ and $\boldsymbol{\beta}^-_k$. Moreover, $\mathbf{\Sigma}^-_{\beta,k}$ and $\boldsymbol{\beta}^-_k$ are expanded to include initial values of newly introduced carrier-phase biases.

The initial value of a new arc-bias can simply be set to zero with a large initial standard deviation. However, this approach can lead to a poor convergence rate of the estimator, or even worse, the filter may not converge at all in time by considering the limited tracking time between a receiver and a satellite. In order

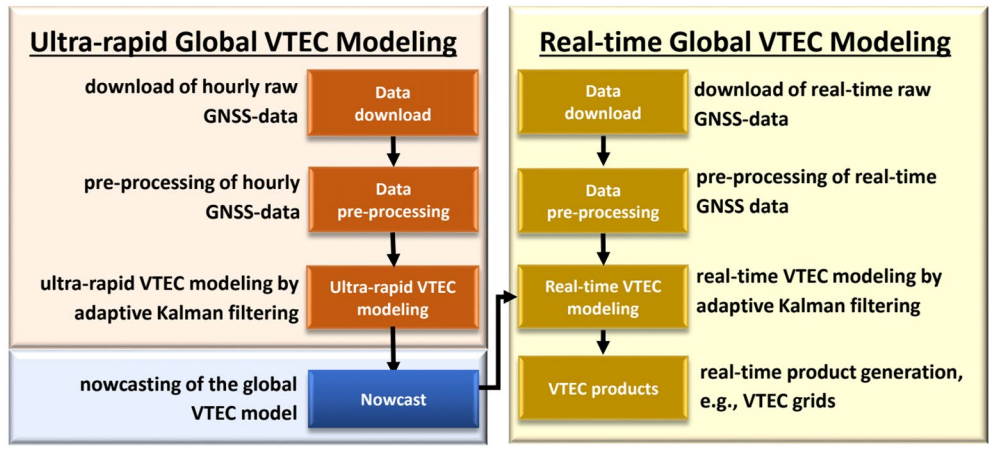

Figure 1. Overall flowchart of the developed real-time modeling approach.

to initialize a new arc-bias, the GNSS measurement Equation 4 with predicted input parameters are used. Accordingly, the initial value $C^{s,0}_{r,\mathrm{GNSS},k}$ reads

$$C^{s,0}_{r,\mathrm{GNSS},k} = y_{\mathrm{GNSS},k} - m(z^s_{r,k}) \cdot VTEC^0_k \tag{21}$$

where $VTEC^0_k$ is computed from the predicted B-spline coefficient vector $\mathbf{d}^-_k$ of the predicted state vector $\boldsymbol{\beta}^-_k$. The initial standard deviation $\sigma_{C^{s,0}_{r,\mathrm{GNSS},k}}$ is approximately obtained by applying the error propagation law to Equation 21 under the assumption that the variables are uncorrelated and reads

$$\sigma_{C^{s,0}_{r,\mathrm{GNSS},k}} \approx \sqrt{\sigma^2_{y_{\mathrm{GNSS},k}} + (m(z^s_{r,k}))^2 \cdot \sigma^2_{VTEC^0_k}}. \tag{22}$$

where $\sigma^2_{y_{\mathrm{GNSS},k}}$ and $\sigma^2_{VTEC^0_k}$ are the variances of the carrier-phase ionospheric observable and the predicted VTEC.

A very small value of the initial standard deviation $\sigma_{C^{s,0}_{r,\mathrm{GNSS},k}}$ can cause the filter to become insensitive to observations in updating the newly introduced arc-bias. A moderate value is commonly desirable in practice for a stable filter convergence. Therefore, the initial standard deviation is multiplied by a user-defined factor. Moreover a random error $e^{s,0}_{r,k}$ derived from a normal distribution, that is, $e^{s,0}_{r,k} \sim N\left(0, \sigma^2_{C^{s,0}_{r,\mathrm{GNSS},k}}\right)$ is added to $C^{s,0}_{r,\mathrm{GNSS},k}$.

The validity of each carrier-phase bias is checked before the measurement update step at every filter cycle. The cleaning and initialization procedures are executed when broken carrier-phase biases are detected or new biases are introduced.

4.3. Overall Real-Time Modeling Algorithm

The flowchart in Figure 1 shows the different steps of the presented real-time modeling approach. The overall procedure can be classified into three main categories labeled by different colors in Figure 1; ultra-rapid VTEC product generation, nowcasting of the global VTEC, and real-time VTEC modeling.

First, hourly GNSS raw data is downloaded from the data centers in RINEX format. Ionosphere observations are extracted from the raw data in the ultra-rapid data pre-processing step. The observations are incorporated into the global VTEC model by the adaptive Kalman filter implementation to generate the ultra-rapid VTEC product labeled as"othg"; see Erdogan et al. (2020) for the computation and implementation details and Goss et al. (2019) for the naming of the product. Following the ultra-rapid product generation, after each hour, the coefficients of the nowcast model (Equation 9) are estimated for each of the global B-spline coefficients. The nowcast model is then executed to obtain the extrapolated B-spline coefficients at the present time (nowcasting). These nowcasted B-spline coefficients are used to feed the real-time VTEC model.

In parallel to the ultra-rapid product generation and the nowcasting processes, real-time GNSS data are continuously downloaded in the RTCM format. As mentioned earlier, 10 s of data sampling are applied to download raw GNSS data. In the real-time data processing step, carrier-phase observations are extracted from the raw data set. Phase-continuous arcs between receivers and satellites are constructed by checking cycle slips and data gaps. Then the ionosphere combination of carrier-phase observations (Equation 3) are computed.

In the next step, the real-time VTEC modeling, the validity of each carrier-phase bias in the state vector is checked in the data editing process before incorporating the observations into the filter; outdated bias parameters are removed, and new biases are introduced into the filter state vector and its covariance matrix. After that, the ionospheric target parameters consisting of the B-spline coefficients and the carrier-phase biases are estimated sequentially using the real-time adaptive Kalman filter. It should be noted that the filter temporal step size is set to 30 s by taking computational resources into account, though the data download rate and the pre-processing step size are set to 10 s.

In the final step, the VTEC product generation in the desired form, for example, grid VTEC maps in IONEX format, are created from the estimated B-spline coefficients (Erdogan et al., 2017; Goss, Hernández-Pajares, et al., 2020).

In the ultra-rapid and real-time models, the criteria taken into account for selecting the resolution levels are essentially based on the distribution of the input data, the computational load, and the desired level of smoothness for the B-spline representation embedded into a Kalman filter (Erdogan et al., 2017, 2020). Accordingly, in this paper, the B-spline level values are set to $J_1 = 5$ and $J_2 = 3$ in Equation 7, leading to a total number of 816 time-dependent B-spline series coefficients updated at each cycle of the filter. The chosen values refer to maximum spherical harmonics degrees of 33 in latitude direction and 12 in longitude direction (Goss et al., 2019).

In the current implementation, one cycle of the sequential modeling approach involving the real-time data download, pre-processing, filtering, and product creation is accomplished in less than a minute.

5. Results and Discussion

The quality assessment and validation of the VTEC products derived by the proposed real-time approach are carried out using (a) the dSTEC analysis and (b) altimeter VTEC comparisons. The dSTEC analysis offers a precise method for validating VTEC over areas with installed GNSS receivers and has been widely used for quality assessments of VTEC products generated by various analysis centers; see, for example, Feltens et al. (2011), Hernández-Pajares et al. (2017), Rovira-Garcia et al. (2015). The abbreviation dSTEC refers to difference of a STEC observation with respect to a reference STEC with highest elevation angle on the same phase-continuous arc. VTEC observations acquired from the altimetry missions allow for validating and comparing VTEC maps over the oceans and have been in use for decades to assess VTEC products provided by the IGS analysis centers (Hernández-Pajares et al., 2009; Roma-Dollase et al., 2018).

The test data set comprises GNSS data from real-time streams collected between October 17 and 21, 2019 for the global VTEC modeling. Altimetry VTEC from the Jason-3 mission and additional GNSS data for the dSTEC analysis were also collected for the same period to validate and evaluate the results.

5.1. Internal Evaluation of VTEC Models

The growing number of receivers providing real-time and hourly data enhance the data distribution spatially. The GNSS receivers are usually operated as part of a network. The networks are designed to provide data covering the globe, such as the IGS network, or a region such as the EUREF network. The quality of the data distribution depends on the geographical distribution and density of receivers in a network.

The top and mid panels of Figure 2 show snapshot VTEC maps with the ionospheric pierce points of the measurements used for the ultra-rapid and real-time models, respectively. Their difference maps are also illustrated in the bottom panels. The maps on the left refer to 10:00 UTC at October 19, 2019, whereas the right side is for 18:00 UTC of the same day. The ultra-rapid approach uses hourly data collected from the IGS

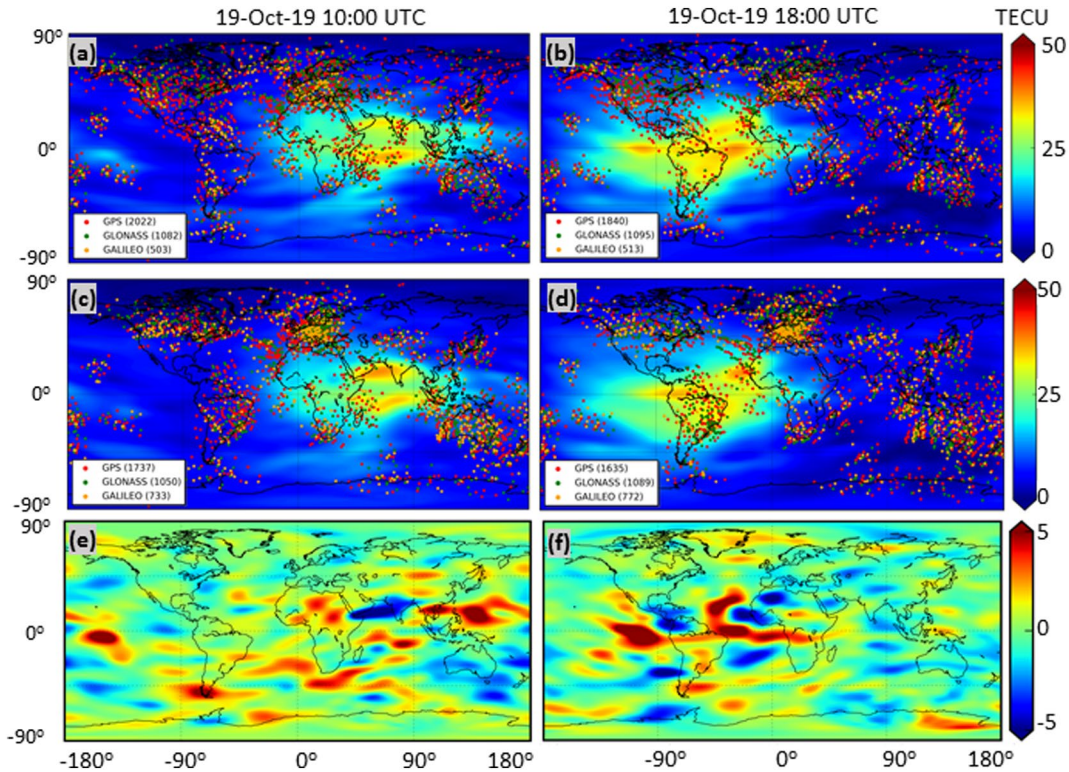

Figure 2. Global Vertical Total Electron Content (VTEC) maps with ionospheric pierce points computed from GPS (red), GLONASS (green), and GALILEO (orange) at 10:00 (left) and 18:00 (right) UTC October 19, 2019: (a and b) maps from ultra-rapid VTEC modeling, (c and d) maps from the presented real-time VTEC modeling approach, and (e and f) their difference maps.

network, and its data distribution is enhanced with an additional hourly data set from manually selected receivers belonging to the UNAVCO and the EUREF networks; see the top panels of Figure 2. For example, additional data from the UNAVCO network mainly cover the Southern United States, Central America, Mexico, and Alaska. In the current implementation, the real-time model is only fed by the data from the receivers contributing to the IGS real-time service. However, the real-time model has more data over Brazil compared to the ultra-rapid model. The receivers in this region contribute to the IGS real-time service; but, no data was available in the hourly data set from IGS data centers.

As shown in the difference maps in Figure 2, the deviations between the ultra-rapid and real-time models are dependent on the VTEC magnitude and the data distribution. For instance, considerable deviations exist over Central America (for 18:00 UTC) and Indian (for 10:00 UTC) regions. A considerable deviation during a high geomagnetic activity between the two models is also expected over the Siberian region due to the data gap in the real-time model; however, it does not become significant for the test period. The real-time model performs well compared to the ultra-rapid model over Europe, where both approaches are fed with dense data, and the differences between the two models are close to zero.

It should also be mentioned that the amount of extracted ionospheric information from raw data also depends on the data pre-processing method. The ultra-rapid approach utilizes the phase-leveling method and requires a minimum of a 30-min length of consecutive code and carrier-phase measurements on the same arc between a receiver and a satellite. The measurements that are part of the short arcs are discarded in ultra-rapid modeling. However, the real-time data pre-processing, which is only based on carrier-phase measurements, does not require such a long arc length in the real-time data pre-processing step. The initialization of a phase-continuous arc is set to a minimum of 2-min, allowing for extracting more ionospheric measurements from GNSS satellites.

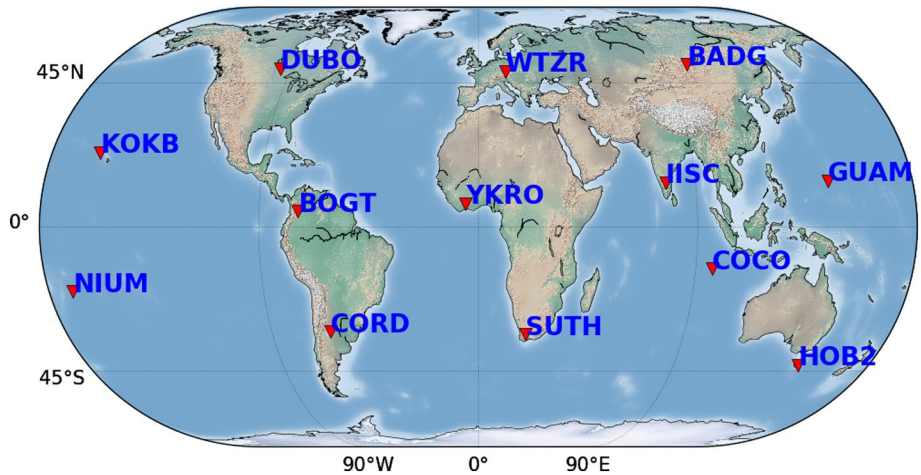

Figure 3. The geographical distribution of the selected Global Navigation Satellite Systems receivers for the differential slant total electron content analysis.

5.2. External Quality Assessment of the Real-Time VTEC Products

There are numerous ongoing experimental efforts for providing real-time products, such as real-time clock and orbit corrections for GPS and GLONASS as well as VTEC maps, provided by IGS; see, for example, Li et al. (2020) for combined VTEC maps. The real-time VTEC products of the Universitat Politècnica de Catalunya (UPC), Spain, and the Chinese Academy of Sciences (CAS), China, in the IONEX format are used in the comparisons to assess the relative performance of the VTEC maps generated in this study. The VTEC products of UPC and CAS will respectively be labeled "uadg" and "rt_casg", and the VTEC maps produced using the developed approach will be labeled "orhg" in the remainder of the paper. The ultra-rapid VTEC product of DGFI-TUM with the label "othg" and the rapid VTEC product of UPC with the label "uqrg", which provide both high spectral resolution, accuracy and temporal resolution, are also included in the analysis for the evaluation of the results. It should be noted that the real-time data dissemination format can change the quality of VTEC products. For example, a conversion of the VTEC product into a spherical harmonic representation complying with the RTCM format drastically decreases the accuracy of high-resolution products since the RTCM 3.x format allows VTEC representation by spherical harmonic expansions only up to a degree 16 (Goss, Hernández-Pajares, et al., 2020). Therefore, VTEC grids in the IONEX format were preferred to avoid such quality degradation for a fair evaluation of the results.

Figure 3 shows the geographical distribution of the GNSS receivers used in the dSTEC analysis. The receivers are selected to reveal the performance of the products according to the VTEC activity showing significant variations with respect to geographic locations and time, such as the Equatorial Ionization Anomaly. The RMS deviations derived from the dSTEC analysis for each test receiver are depicted in Figure 4. The

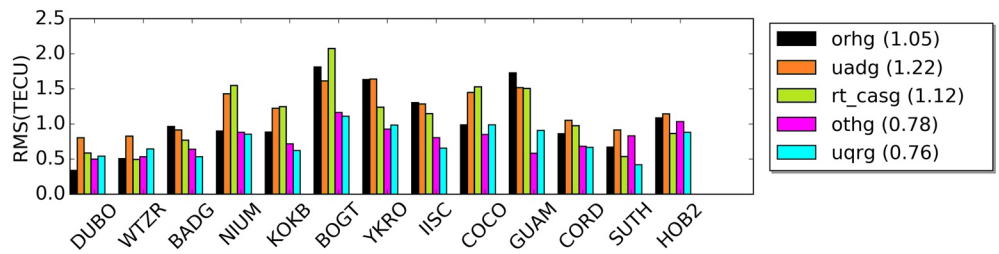

Figure 4. RMS values from the differential slant total electron content analysis at the Global Navigation Satellite System stations depicted in Figure 3. The results refer to the data sets covering the days between October 17 (DOY 290) and October 21 (DOY 294) of 2019. The label "orhg" stands for the presented real-time approach. The labels "uadg" and "rt_casg" refer to the real-time UPC and CAS products, "othg" and "uqrg" stand for the ultra-rapid DGFI-TUM product and the rapid UPC product.

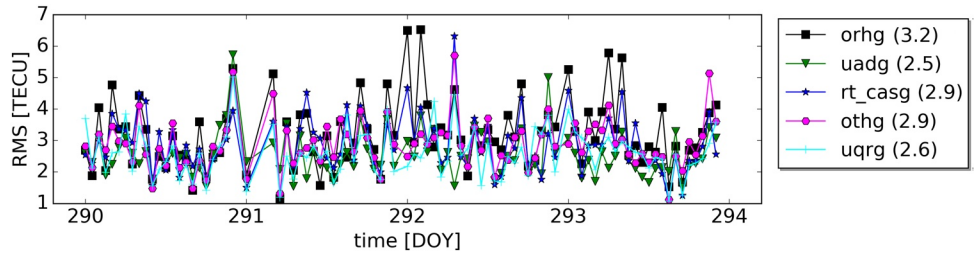

Figure 5. RMS values computed for each hour from Jason-3 altimetry comparisons. The results refer to the data sets covering the days between October 17 (DOY 290) and October 21 (DOY 294) of 2019. The label "orhg" stands for the presented real-time approach. The labels "uadg" and "rt_casg" refer to the real-time UPC and CAS products, "othg" and "uqrg" stand for the ultra-rapid DGFI-TUM product and the rapid UPC product.

legend in the right panel shows the average values of the RMS deviations for each analysis center. The average RMS deviations in Figure 4 are ranging from 0.76 to 1.22 TECU. The values reveal that the quality of the real-time VTEC product "orhg" is in line with those from the other analysis centers. The accuracy of "orhg" with RMS deviation of 1.05 TECU is slightly better than the real-time VTEC products of "uadg" and "rt_casg" during the test period. The biases, which reveal the systematic variations between the VTEC solutions, are not illustrated in the figure but range from −0.05 to 0.02 TECU for the test period. The real-time product "orhg" has an average bias of −0.01 TECU. The (ultra) rapid VTEC solutions "othg" and "uqrg" show superior performance than the real-time solutions by means of the RMS deviations. This performance can be associated with better data distribution. Noticeable quality degradation for all products is visible for the GNSS receivers located around the geomagnetic equator and is significantly larger for the real-time products than the rapid products; see the RMS deviations for the receivers NIUM, KOKB, BOGT, YKRO, IISC, and GUAM in Figure 4. This degradation is usually attributed to a lack of enough data coverage and VTEC activity at large magnitudes, which occurs at regions around the geomagnetic equator.

Furthermore, VTEC observations obtained from the dual-frequency altimeter of Jason-3 mission were used to evaluate the performance of generated VTEC maps over the oceans. Although VTEC data from satellite altimetry typically suffer from calibration biases that can reach up-to several TECU (Azpilicueta & Brunini, 2009) and pronounced noise (Hernández-Pajares et al., 2017), it provides a direct and independent way to evaluate VTEC maps (Roma-Dollase et al., 2018; Li et al., 2020). A pre-filtering is usually applied to smooth noisy raw altimetry observations (see, e.g., Li et al., 2020; Hernández-Pajares et al., 2017). In this study, a median filter with a window size of 20 s was carried out to smooth the raw data and discard outliers (see, Erdogan et al., 2017). Since the temporal sampling of Jason-3 data is higher than the VTEC products, a tri-linear spatio-temporal interpolator was performed in the Sun-fixed coordinate system to compute VTEC values from the maps for the corresponding time and location of the altimetry observations.

The RMS of the differences between altimetry VTEC observations and the corresponding VTEC model values derived from products of each analysis center are used as a metric for the relative quality assessment. The RMS values of the differences computed for each hour for the test period are depicted in Figure 5. The results reveal that the average RMS values, given in the legend of the figure, for each product vary in a range between 2.5 and 3.2 TECU. The RMS value of the real-time solution "orhg" for the corresponding data sets is 3.2 TECU, and it is in compliance, considering the precision level of the altimetry observations, with those of the real-time products "uadg" and "rt_casg", which are 2.5 and 2.9 TECU, respectively. Additionally, among the real-time products, "uadg" has the smallest average bias of 0.5 TECU, whereas the "orhg" and "rt_casg" solutions have 0.8 TECU for the test period. In the current implementation, the presented approach focuses on continental areas, where the model accuracy is superior compared to the marine areas. The slight under-performance of the B-spline approach over the oceans according to the RMS deviations can be attributed to the compact support of its basis functions compared to spherical harmonics, which provide an averaging effect over the globe. However, the accuracy over the marine areas can be improved by incorporating additional GNSS receivers established on islands and coasts from reliable networks. Furthermore, by adapting methods based on interpolations into ionosphere modeling, significant performance improvements over large data gaps can be achieved. For instance, the rapid "uqrg" product of UPC makes

use of Kriging interpolation and the real-time product "uadg" employs a method called Atomic Decomposition Interpolator of GIMs (ADIGIM); see, for example, Yang et al. (2021).

6. Conclusions

This paper focuses (a) on embedding a B-spline representation of the global VTEC into a Kalman filter running in real-time, (b) on utilizing exclusively carrier-phase observations acquired from GPS, GLONASS, and GALILEO via the real-time data streams, and (c) on simultaneously estimating the unknown target parameters comprising the B-spline coefficients and the carrier-phase biases.

According to Erdogan et al. (2017, 2020), incorporating the global VTEC B-spline representation (Schmidt et al., 2015) into an adaptive Kalman filter results in an efficient recursive data ingestion framework for ultra-rapid modeling. This adaptive modeling approach was extended to real-time in the frame of this paper to exploit the efficient heterogeneous data handling capability and the localizing property of B-splines. Besides, the localizing feature of the B-spline functions results in highly sparse structures in the design matrix of the filter measurement model. By considering the large scale and sparsity of the problem, sparse matrix techniques were introduced for the matrix/vector operations in the filter measurement update step. This adaptation significantly decreased the filter computation time, which is a critical matter for real-time VTEC modeling. In the current implementation, one cycle of the real-time processes, including the filtering step, takes less than a minute.

The measurement model of the presented approach is based on the geometry-free combination of carrier-phase observations, which is composed of an ionospheric signal term and a combined bias term. Instead of eliminating them in a data pre-processing step, all carrier-phase biases are estimated along with the B-spline coefficients in run-time. The advantage of the approach is that it does not require the use of code observations compared to the conventional carrier-phase leveling technique. Furthermore, the geometry-free combination does not require precise auxiliary data (such as precise orbit and clock products) contrary to methods for extracting ionosphere parameters from PPP-based solutions. Low latency and moderate-quality ultra-rapid orbits, which include predicted satellite positions and clock biases, are used to compute, for instance, ionosphere pierce-points and elevation angles of observations. On the other hand, these advantages come at the expense of estimating a large number of unknown carrier-phase biases, which are about 3,500 parameters in addition to the 816 B-spline coefficients at each epoch for the test period. However, the ultra-rapid modeling approach based on the phase leveling method requires the estimation of about 600 DCBs in addition to the B-spline coefficients. The large size of the state vector and large data gaps can result in an unstable filter implementation leading to quality degradation of VTEC products. Supplementary information derived from the nowcast model was incorporated into the filter to cope with such a problem.

The performance assessment of the implemented real-time VTEC modeling was carried out via the dSTEC analysis and Jason-3 altimetry VTEC comparisons. The results show that the quality of the real-time VTEC product "orhg" is slightly better in terms of average RMS of 1.05 TECU than the other real-time products, ranging from 1.12 to 1.22 TECU, according to the dSTEC analysis during the test period. Besides, the RMS of 3.2 TECU for the real-time "orhg" product is in close agreement with those, ranging from 2.5 to 2.9 TECU, used in the evaluations with respect to the altimetry VTEC analysis providing a noisy but reliable assessment method over the oceans. Nevertheless, as mentioned before, further performance improvement over the oceans for the product "orhg" is expected by incorporating new receivers from additional GNSS networks and implementing methods based on interpolation. Moreover, considering the rapid advances in technology, if data sets from other space geodetic techniques such as DORIS and satellite altimeter can be provided in real-time, these data can be included in VTEC modeling. This issue will be handled as a follow-up study.

The results encourage further research to extend the measurement model of the real-time Kalman filter to consider additional satellite constellations such as BeiDou. The current implementation of the approach utilizes data from the real-time IGS network. In order to obtain a better data distribution, complementary data sources from reliable real-time networks, for instance, the UNAVCO network, will be introduced. Rapidly enlarging regional networks providing a dense set of GNSS receivers, for instance, the real-time

European network (EUREF), strongly encourage us to apply the presented approach to real-time regional VTEC modeling. The evaluations show that the presented approach has rather promising outcomes during the selected period (October 17–21, 2019). Nevertheless, further tests covering a longer time span and including solar events will be performed as part of a near-future study.

Data Availability Statement

Accessing the real-time GNSS resources from the IGS service (http://igs-ip.net/home) was possible by the open-source BKG Ntrip Client (BNC) software (see, Weber et al., 2016) after the completion of the registration procedure via the web page "https://register.rtcm-ntrip.org/cgi-bin/registration.cgi". The hourly GNSS data used for the dSTEC analysis can be obtained from the archives of IGS data centers, such as CDDIS (via the web portal "https://cddis.nasa.gov/"). The real-time and rapid VTEC GIMs from UPC and the real-time VTEC GIMs from CAS, used in the validation step, are publicly provided through the data repositories of UPC and CAS; see, Yang et al. (2021) and Li et al. (2020) for further information. The created VTEC GIMs based on the presented real-time approach can be accessed through the research data repository of TUM via the link "https://doi.org/10.14459/2021mp1621980". Altimetry data provided by NOAA is available from the website at "https://www.ncei.noaa.gov/data/oceans/jason3/".

Acknowledgments
This work was supported by the German Research Foundation (DFG) and the Technical University of Munich (TUM) in the framework of the Open Access Publishing Program. The approach presented in this study was mainly developed within the project OPTIMAP (Operational Tool for Ionospheric Mapping and Prediction) funded by the Bundeswehr GeoInformation Center (BGIC) and the German Space Situational Awareness Centre (GSSAC). Open access funding enabled and organized by Projekt DEAL.

References

Azpilicueta, F., & Brunini, C. (2009). Analysis of the bias between TOPEX and GPS vTEC determinations. *Journal of Geodesy*, *83*(2), 121–127. https://doi.org/10.1007/s00190-008-0244-7

Banville, S., Langley, R. B., & Brunswick, N. (2011). Defining the basis of an " Integer - Levelling " procedure for estimating slant total electron content. In *Proceedings of the 24th international technical meeting of the satellite division of the institute of navigation (ion gnss 2011)* (pp. 2542–2551). Portland, Oregon.

Banville, S., Zhang, W., Ghoddousi-fard, R., & Langley, R. B. (2012). Ionospheric monitoring using " Integer - Levelled " observations. In *Proceedings of the 25th international technical meeting of the satellite division of the institute of navigation (ion gnss 2012)* (pp. 2692–2701). Nashville, TN.

Brown, R. G., & Hwang, P. Y. C. (2012). *Introduction to random signals and applied Kalman filtering: With MATLAB exercises* (4th ed.). USA: John Wiley & Sons, Inc.

Brunini, C., & Azpilicueta, F. J. (2009). Accuracy assessment of the GPS-based slant total electron content. *Journal of Geodesy*, *83*(8), 773–785. https://doi.org/10.1007/s00190-008-0296-8

Caissy, M., Agrotis, L., Weber, G., Hernandez-Pajares, M., & Hugentobler, U. (2012). *The international GNSS real-time service*. GPS World.

Chen, L., Yi, W., Song, W., Shi, C., Lou, Y., & Cao, C. (2018). Evaluation of three ionospheric delay computation methods for ground-based GNSS receivers. *GPS Solutions*, *22*(4), 125. https://doi.org/10.1007/s10291-018-0788-9

Ciraolo, L., Azpilicueta, F., Brunini, C., Meza, A., & Radicella, S. M. (2007). Calibration errors on experimental slant total electron content (TEC) determined with GPS. *Journal of Geodesy*, *81*(2), 111–120. https://doi.org/10.1007/s00190-006-0093-1

Dettmering, D., Limberger, M., & Schmidt, M. (2014). Using DORIS measurements for modeling the vertical total electron content of the Earth's ionosphere. *Journal of Geodesy*, *88*, 1131–1143. https://doi.org/10.1007/s00190-014-0748-2

Dettmering, D., Schmidt, M., Heinkelmann, R., & Seitz, M. (2011). Combination of different space-geodetic observations for regional ionosphere modeling. *Journal of Geodesy*, *85*(12), 989–998. https://doi.org/10.1007/s00190-010-0423-1

Durmaz, M., & Karslioglu, M. O. (2015). Regional vertical total electron content (VTEC) modeling together with satellite and receiver differential code biases (DCBs) using semi-parametric multivariate adaptive regression B-splines (SP-BMARS). *Journal of Geodesy*, *89*(4), 347–360. https://doi.org/10.1007/s00190-014-0779-8

Erdogan, E., Schmidt, M., Goss, A., Görres, B., & Seitz, F. (2020). Adaptive modeling of the global ionosphere vertical total electron content. *Remote Sensing*, *12*(11), 1822. https://doi.org/10.3390/rs12111822

Erdogan, E., Schmidt, M., Seitz, F., & Durmaz, M. (2017). Near real-time estimation of ionosphere vertical total electron content from GNSS satellites using B-splines in a Kalman filter. *Annales Geophysicae*, *35*(2), 263–277. https://doi.org/10.5194/angeo-35-263-2017

Farzaneh, S., & Forootan, E. (2017). Reconstructing regional ionospheric electron density: A Combined Spherical Slepian Function and Empirical Orthogonal Function Approach. *Surveys in Geophysics*, *39*, 289–309. https://doi.org/10.1007/s10712-017-9446-y

Feltens, J., Angling, M., Jackson-Booth, N., Jakowski, N., Hoque, M., Hernández-Pajares, M., et al. (2011). Comparative testing of four ionospheric models driven with GPS measurements. *Radio Science*, *46*(6), RS0D12. https://doi.org/10.1029/2010RS004584

A. Gelb (Ed.), (1974). *Applied optimal estimation*. Cambridge: The MIT Press.

Gerzen, T., Minkwitz, D., Schmidt, M., & Erdogan, E. (2020). Analysis of different propagation models for the estimation of the topside ionosphere and plasmasphere with an ensemble Kalman filter. *Annales Geophysicae*, *38*(6), 1171–1189. https://doi.org/10.5194/angeo-38-1171-2020

Goss, A., Hernández-Pajares, M., Schmidt, M., Roma-Dollase, D., Erdogan, E., & Seitz, F. (2020). High-resolution ionosphere corrections for single-frequency positioning. *Remote Sensing*, *13*(1), 12. https://doi.org/10.3390/rs13010012

Goss, A., Schmidt, M., Erdogan, E., Görres, B., & Seitz, F. (2019). High resolution vertical total electron content maps based on multi-scale b-spline representations. *Annales Geophysicae Discussions*, *37*, 699–717. https://doi.org/10.5194/angeo-37-699-2019

Goss, A., Schmidt, M., Erdogan, E., & Seitz, F. (2020). Global and regional high-resolution VTEC modelling using a two-step b-spline approach. *Remote Sensing*, *12*(7), 1198. https://doi.org/10.3390/rs12071198

Grewal, M. S., & Andrews, A. P. (2008). *Kalman filtering: Theory and practice using MATLAB* (2nd ed.). Hoboken, New Jersey: John Wiley & Sons, Inc.

Hansen, A. J. (1998). Real-time ionospheric tomography using terrestrial GPS sensors. In *Proceedings of the 11th international technical meeting of the satellite division of the institute of navigation (ion gps 1998)* (pp. 717–727). Nashville, TN.
Hernández-Pajares, M., Juan, J., & Sanz, J. (1999). New approaches in global ionospheric determination using ground GPS data. *Journal of Atmospheric and Solar-Terrestrial Physics*, *61*(16), 1237–1247. https://doi.org/10.1016/S1364-6826(99)00054-1
Hernández-Pajares, M., Juan, J. M., Sanz, J., Aragón-Àngel, À., García-Rigo, A., Salazar, D., & Escudero, M. (2011). The ionosphere: Effects, GPS modeling and the benefits for space geodetic techniques. *Journal of Geodesy*, *85*(12), 887–907. https://doi.org/10.1007/s00190-011-0508-5
Hernández-Pajares, M., Juan, J. M., Sanz, J., Orus, R., Garcia-Rigo, A., Feltens, J., et al. (2009). The IGS VTEC maps: A reliable source of ionospheric information since 1998. *Journal of Geodesy*, *83*(3–4), 263–275. https://doi.org/10.1007/s00190-008-0266-1
Hernández-Pajares, M., Roma-Dollase, D., Krankowski, A., García-Rigo, A., & Orús-Pérez, R. (2017). Methodology and consistency of slant and vertical assessments for ionospheric electron content models. *Journal of Geodesy*, *91*(12), 1405–1414. https://doi.org/10.1007/s00190-017-1032-z
Hide, C., Moore, T., & Smith, M. (2004). Adaptive Kalman filtering algorithms for integrating GPS and low cost INS. In *Plans 2004. Position location and navigation symposium (ieee cat. no.04ch37556)* (pp. 227–233). IEEE. https://doi.org/10.1109/PLANS.2004.1308998
Hofmann-Wellenhof, B., Lichtenegger, H., & Wasle, E. (2008). *GNSS – global navigation satellite systems. GPS, GLONASS, Galileo, and more*. Wien: Springer Verlag.
Jazwinski, A. H. (2007). *Stochastic processes and filtering theory*. Mineola, New York: Dover Publications, Inc.
Jerez, G. O., Hernández-Pajares, M., Prol, F. S., Alves, D. B. M., & Monico, J. F. G. (2020). Assessment of global ionospheric maps performance by means of ionosonde data. *Remote Sensing*, *12*(20), 3452. https://doi.org/10.3390/rs12203452
Kalman, R. (1960). A new approach to linear filtering and prediction problems. *Journal of Basic Engineering*, *82*(1), 35–45. https://doi.org/10.1115/1.3662552
Koch, K. R. (1999). *Parameter estimation and hypothesis testing in linear models*. Springer.
Krypiak-Gregorczyk, A., & Wielgosz, P. (2018). Carrier phase bias estimation of geometry-free linear combination of GNSS signals for ionospheric TEC modeling. *GPS Solutions*, *22*(2), 45. https://doi.org/10.1007/s10291-018-0711-4
Krypiak-Gregorczyk, A., Wielgosz, P., & Borkowski, A. (2017). Ionosphere model for European region based on Multi-GNSS data and TPS interpolation. *Remote Sensing*, *9*(12), 1221. https://doi.org/10.3390/rs9121221
Laundal, K. M., & Richmond, A. D. (2016). Magnetic coordinate systems. *Space Science Reviews*, *206*, 27–59. https://doi.org/10.1007/s11214-016-0275-y
Li, Z., Wang, N., Hernández-Pajares, M., Yuan, Y., Krankowski, A., Liu, A., et al. (2020). IGS real-time service for global ionospheric total electron content modeling. *Journal of Geodesy*, *94*(3), 32. https://doi.org/10.1007/s00190-020-01360-0
Liang, W., Limberger, M., Schmidt, M., Dettmering, D., Hugentobler, U., Bilitza, D., et al. (2015). Regional modeling of ionospheric peak parameters using GNSS data—An update for IRI. *Advances in Space Research*, *55*(8), 1981–1993. https://doi.org/10.1016/j.asr.2014.12.006
Limberger, M. (2015). *Ionosphere modeling from GPS radio occultations and complementary data based on B-splines* (Dissertation, Technischen Universität München, Munich). Retrieved from https://mediatum.ub.tum.de/doc/1254715/1254715
Limberger, M., Liang, W., Schmidt, M., Dettmering, D., & Hugentobler, U. (2013). Regional representation of F2 Chapman parameters based on electron density profiles. *Annales Geophysicae*, *31*(12), 2215–2227. https://doi.org/10.5194/angeo-31-2215-2013
Liu, T., Zhang, B., Yuan, Y., & Li, M. (2018). Real-time precise point positioning (RTPPP) with raw observations and its application in real-time regional ionospheric VTEC modeling. *Journal of Geodesy*, *92*(11), 1267–1283. https://doi.org/10.1007/s00190-018-1118-2
Liu, Z. (2004). *Ionosphere tomographic modeling and applications using global positioning system (GPS) measurements*. (PhD. dissertation). University of Calgary. https://doi.org/10.11575/PRISM/17654
Lyche, T., & Schumaker, L. L. (2000). A multiresolution tensor spline method for fitting functions on the sphere. *SIAM Journal on Scientific Computing*, *22*(2), 724–746. https://doi.org/10.1137/S1064827598344388
Mannucci, A. J., Wilson, B. D., & Edwards, C. D. (1993). A new method for monitoring the Earth's ionospheric total electron content using the GPS global network. In *Proceedings of the 6th international technical meeting of the satellite division of the institute of navigation (ion gps 1993)* (pp. 1323–1332). Salt Lake City, UT.
Mannucci, A. J., Wilson, B. D., Yuan, D. N., Ho, C. H., Lindqwister, U. J., & Runge, T. F. (1998). A global mapping technique for GPS-derived ionospheric total electron content measurements. *Radio Science*, *33*(3), 565–582. https://doi.org/10.1029/97RS02707
Mehra, R. (1972). Approaches to adaptive filtering. *IEEE Transactions on Automatic Control*, *17*(5), 693–698. https://doi.org/10.1109/TAC.1972.1100100
Nohutcu, M., Karslioglu, M., & Schmidt, M. (2010). B-spline modeling of VTEC over Turkey using GPS observations. *Journal of Atmospheric and Solar-Terrestrial Physics*, *72*(7–8), 617–624. https://doi.org/10.1016/j.jastp.2010.02.022
Ren, X., Chen, J., Li, X., & Zhang, X. (2020). Ionospheric Total Electron Content Estimation Using GNSS Carrier Phase Observations Based on Zero-Difference Integer Ambiguity: Methodology and Assessment. *IEEE Transactions on Geoscience and Remote Sensing*, *59*, 817–830. https://doi.org/10.1109/TGRS.2020.2989131
Ren, X., Chen, J., Li, X., Zhang, X., & Freeshah, M. (2019). Performance evaluation of real-time global ionospheric maps provided by different IGS analysis centers. *GPS Solutions*, *23*(4), 113. https://doi.org/10.1007/s10291-019-0904-5
Roma-Dollase, D., Hernández-Pajares, M., Krankowski, A., Kotulak, K., Ghoddousi-Fard, R., Yuan, Y., et al. (2018). Consistency of seven different GNSS global ionospheric mapping techniques during one solar cycle. *Journal of Geodesy*, *92*(6), 691–706. https://doi.org/10.1007/s00190-017-1088-9
Rovira-Garcia, A., Juan, J. M., Sanz, J., & Gonzalez-Casado, G. (2015). A worldwide ionospheric model for fast precise point positioning. *IEEE Transactions on Geoscience and Remote Sensing*, *53*(8), 4596–4604. https://doi.org/10.1109/TGRS.2015.2402598
Rovira-Garcia, A., Juan, J. M., Sanz, J., González-Casado, G., & Ibáñez, D. (2016). Accuracy of ionospheric models used in GNSS and SBAS: Methodology and analysis. *Journal of Geodesy*, *90*(3), 229–240. https://doi.org/10.1007/s00190-015-0868-3
Schaer, S. (1999). *Mapping and predicting the Earth's ionosphere using the global positioning system*. (Dissertation). Bern: University of Bern.
Schmidt, M. (2007). Wavelet modelling in support of IRI. *Advances in Space Research*, *39*(5), 932–940. https://doi.org/10.1016/j.asr.2006.09.030
Schmidt, M. (2012). Towards a multi-scale representation of multi-dimensional signals. In N. Sneeuw, P. Novák, M. Crespi, & F. Sansò (Eds.), *Vii hotine-marussi symposium on mathematical geodesy, international association of geodesy symposia* (Vol. 137, pp. 119–127). Berlin, Heidelberg: Springer Berlin Heidelberg. https://doi.org/10.1007/978-3-642-22078-4_18
Schmidt, M., Bilitza, D., Shum, C., & Zeilhofer, C. (2008). Regional 4-D modeling of the ionospheric electron density. *Advances in Space Research*, *42*(4), 782–790. https://doi.org/10.1016/j.asr.2007.02.050

Schmidt, M., Dettmering, D., Mößmer, M., Wang, Y., & Zhang, J. (2011). Comparison of spherical harmonic and B spline models for the vertical total electron content. *Radio Science*, *46*(6), RS0D11. https://doi.org/10.1029/2010RS004609

Schmidt, M., Dettmering, D., & Seitz, F. (2015). Using B-spline expansions for ionosphere modeling. In W. Freeden, M. Z. Nashed, & T. Sonar (Eds.), *Handbook of geomathematics* (pp. 939–983). Berlin, Heidelberg: Springer Berlin Heidelberg. https://doi.org/10.1007/978-3-642-54551-1_80

Schumaker, L. L., & Traas, C. (1991). Fitting scattered data on spherelike surfaces using tensor products of trigonometric and polynomial splines. *Numerische Mathematik*, *60*(1), 133–144. https://doi.org/10.1007/BF01385718

Simon, D. (2010). Kalman filtering with state constraints: A survey of linear and nonlinear algorithms. *IET Control Theory & Applications*, *4*(8), 1303–1318. https://doi.org/10.1049/iet-cta.2009.0032

Skone, S. (1999). *Wide area ionosphere grid modelling in the auroral region*. (Ph.D. Thesis). University of Calgary.

Subirana, J. S., Zornoza, J. M. J., & Hernandez-Pajares, M. (2013). *GNSS data processing, vol. 1: Fundamentals and algorithms* (Vol. I). ESA Communications.

Teixeira, B. O., Chandrasekar, J., Tôrres, L. A., Aguirre, L. A., & Bernstein, D. S. (2009). State estimation for linear and non-linear equality-constrained systems. *International Journal of Control*, *82*(5), 918–936. https://doi.org/10.1080/00207170802370033

Weber, G., Dettmering, D., & Gebhard, H. (2005). Networked transport of rtcm via internet protocol (NTRIP). In *A window on the future of geodesy* (pp. 60–64). Berlin/Heidelberg: Springer-Verlag. https://doi.org/10.1007/3-540-27432-4_11

Weber, G., Mervart, L., Stürze, A., Rülke, A., & Stöcker, D. (2016). *BKG Ntrip Client. Frankfurt am Main: Mitteilungen des Bundesamtes für Kartographie und Geodäsie*. Retrieved from https://igs.bkg.bund.de/ntrip/bnc

Xiang, Y., Gao, Y., Shi, J., & Xu, C. (2017). Carrier phase-based ionospheric observables using PPP models. *Geodesy and Geodynamics*, *8*(1), 17–23. https://doi.org/10.1016/j.geog.2017.01.006

Xiang, Y., Gao, Y., Shi, J., & Xu, C. (2019). Consistency and analysis of ionospheric observables obtained from three precise point positioning models. *Journal of Geodesy*, *93*(8), 1161–1170. https://doi.org/10.1007/s00190-019-01233-1

Yang, H., Monte-Moreno, E., Hernández-Pajares, M., & Roma-Dollase, D. (2021). Real-time interpolation of global ionospheric maps by means of sparse representation. *Journal of Geodesy*, *95*(6), 71. https://doi.org/10.1007/s00190-021-01525-5

Zeilhofer, C., Schmidt, M., Bilitza, D., & Shum, C. (2009). Regional 4-D modeling of the ionospheric electron density from satellite data and IRI. *Advances in Space Research*, *43*(11), 1669–1675. https://doi.org/10.1016/j.asr.2008.09.033

Zhang, B. (2016). Three methods to retrieve slant total electron content measurements from ground-based GPS receivers and performance assessment. *Radio Science*, *51*(7), 972–988. https://doi.org/10.1002/2015RS005916